Robustness and scattering behavior of topological phonons in crystalline materials

Zhong-Ke Ding, Yu-Jia Zeng, Hui Pan, Nannan Luo, Li-Ming Tang,* Jiang Zeng,† and Ke-Qiu Chen‡
Department of Applied Physics, School of Physics and Electronics, Hunan University, Changsha 410082, China

(Received 8 December 2023; revised 20 April 2024; accepted 17 May 2024; published 3 June 2024)

Topologically protected edge states of phonons are commonly believed to be immune to backscattering according to previous theoretical works. However, the scattering behavior of the numerous topological phonon (TP) states discovered in natural crystalline materials in recent years has not been concretely examined. In the present work, our analysis of the spring model device shows that the topologically protected phonon edge mode will also be scattered if a suitable backscattering channel is constructed. Based on atomistic S-matrix method, we extend phonon band unfolding technique and explore the robustness of TP transport in zigzag graphene nanoribbon (ZGNR) device through first-principles calculation. Our results show that TP edge states in ZGNR experience strong scattering because the bulk phonon modes provide backscattering channels for TPs in the local band gaps. These computational results indicate that topological phonon edge states located within local band gaps, in ZGNRs or even in other nanomaterials, may not exhibit the robustness as expected. Exploring TP states within natural full band gaps of crystalline materials may present a more effective strategy for mitigating backscattering challenges.

DOI: 10.1103/PhysRevB.109.245104

I. INTRODUCTION

Topological phononics has been garnering significant interest as an analog to topological electronics due to its intriguing characteristics [1–11]. In recent years, as researchers delve deeper into this field, an ever-growing number of topological phonon (TP) states have been discovered in various natural crystalline materials. Similar to the topological classifications in electronic systems, TPs in crystalline materials can been theoretically categorized into several distinct types, including Dirac phonons [12–14], Weyl phonons [15–18], nodal-line phonons [19–21], nodal-ring phonons [22,23], topological acoustic phonons [24–26], high-order TPs [27], and so on. The existence of these diverse TP states has heightened expectations for their potential applications in phonon devices [6,28,29], topological transport [30–35], magnon-phonon coupling [36–38], non-Hermitian topology [39,40], twisted materials [41,42], and so on.

Due to the distinct statistical properties of phonons compared to electrons, there is no concept of Fermi surface in phonon band structures [9]. Therefore, unlike topological insulators in electronic systems, when a system possesses topologically protected phonon surface states, its bulk phonon modes still participate in phonon transport. In previous works, it has been proved that in honeycomb spring model lattice, the TP edge modes remain highly robust than bulk modes [2,6,7,30]. These TP modes are located within full band gaps (FBGs), where FBG refer to band gap that exists throughout the entire Brillouin zone. However, in the process of transport of TP edge modes, the presence of bulk phonon modes may introduce some additional scattering, especially when the TP modes are located in a local band gap (LBG) of the phonon spectrum [13,15,17,19,20,26]. The LBG here signifies the presence of a band gap only within a specific range of wave vectors in the Brillouin zone. It need to be mentioned that the TPs in crystalline materials are typically found in the LBG of the phonon spectrum due to the lack of an efficient mechanism to break the time-reversal symmetry and open a full band gap. Therefore, in crystalline materials, the robustness of TP edge states in transport process needs to be reassessed.

In this work, we quantitatively investigate the transmission of every individual TP edge states during the phonon transport process. The computational analysis of spring mode devices shows the scattering mechanism of TP edge mode during transport. Intuitively, when there are suitable backscattering channels, the topologically protected edge states of phonons can also be scattered. Furthermore, taking zigzag graphene nanoribbon as an example [13,26], we investigate transport behaviors of every individual TP mode located within LBGs. Here, we extend phonon band unfolding technique based on the S-matrix method [43,44], so that it is possible to show the transmission coefficient of every TP in LBGs. Our result shows that bulk phonon modes create backscattering channels for TPs, leading to increased scattering of TP states in zigzag graphene nanoribbon (ZGNRs) compared to bulk phonon modes. Therefore, the expected strong robustness of TP edge states within LBGs, whether in graphene nanoribbons (GNRs) or other nanomaterials, may not be valid.

II. TWO-DIMENSIONAL SPRING MODEL DEVICES

To begin, let us take 2D phonon devices as an example for the investigation of transport behaviors exhibited by TP states. The atomistic Green's function method is usually used to provide the phonon transmission $\Xi(\omega)$ as a function of ω

*lmtang@semi.ac.cn
†jiangzeng@hnu.edu.cn
‡Corresponding author: keqiuchen@hnu.edu.cn

 ©2024 American Physical Society

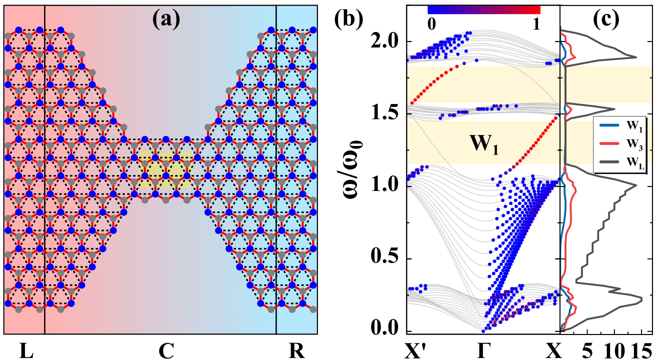

FIG. 1. Device transmission spectrum of honeycomb lattice. (a) Schematic of the two-dimensional device constructed from honeycomb lattice. Blue and gray points represent the sublattices with masses m_A and $m_B = m_A$, respectively. The red solid line and the black dashed line represent massless springs with stiffness k_1 and $k_2 = 0.05k_1$, respectively. The time-reversal ($\mathcal{T}$) symmetry is broken by introducing gyroscopic coupling [2]. (b) Mode-resolved transmission spectrum of the phonon modes from the left lead to the right lead. (c) Total transmission coefficient Ξ of the phonon modes from the left lead as a function of ω.

through the Caroli formula [45,46]. In order to assess the transmission of every individual phonon mode, the atomistic S-matrix method proves to be an effective research tool [43,44,47,48]. Using this method, we can obtain the flux-normalized transmission matrix $\boldsymbol{t}$ for phonon transmission from the left lead to the right lead [see Supplemental Material [49] for more details]. The matrix element $t_{m,n}$ represents the transmission amplitude of mode n from the left thermal lead to mode m of the right thermal lead. Therefore, by summing across all phonon channels in the right thermal lead, we can obtain the transmission coefficient (TC) of mode n from the left thermal lead, as follows:

$$\Xi_n^L(\omega) = \sum_m |t_{m,n}|^2. \tag{1}$$

Next, we consider a 2D phonon device shown in Fig. 1(a). The device is constructed from a classic harmonic honeycomb lattice. Here, the theoretical framework for lattice interactions is drawn from the results presented in Ref. [2]. By introducing gyroscopic coupling into this system, the time-reversal ($\mathcal{T}$) symmetry is broken. The phonon modes of the leads can be described using the eigenvalue equation

$$[\tilde{\mathbf{M}}^{-1/2}\mathbf{K}(\mathbf{q})\tilde{\mathbf{M}}^{-1/2} - \omega^2]\mathbf{U} = 0, \tag{2}$$

where ω and $\mathbf{U}$ represent the eigenfrequency and eigenstate, respectively. $\mathbf{K}$ is the stiffness matrix as a function of Bloch wave vector $\mathbf{q}$ and $\tilde{\mathbf{M}}$ is the mass matrix which has the following form:

$$\tilde{\mathbf{M}} = \begin{pmatrix} \tilde{\mathbf{M}}_\mathbf{1} & 0 & 0 \\ 0 & \ddots & 0 \\ 0 & 0 & \tilde{\mathbf{M}}_\mathbf{N} \end{pmatrix}. \tag{3}$$

The gyroscopic coupling is included through the mass matrix. Reference [2] shows the matrix element of $\tilde{\mathbf{M}}$:

$$\tilde{\mathbf{M}}_\nu = \begin{pmatrix} m_\nu & i\alpha_\nu \\ -i\alpha_\nu & m_\nu \end{pmatrix}. \tag{4}$$

For simplicity, we assume that the AB sublattices in a honeycomb lattice primitive cell have the same mass matrix, i.e., $m_A = m_B = 1$ and $\alpha_A = \alpha_B = 0.3$, where α represent the spinner constant of the gyroscope. Besides, the red solid line and the black dashed line in Fig. 1(a) represent linear springs with stiffness values of $k_1 = 1$ and $k_2 = 0.05$, respectively.

To assess the robustness of the topological edge state of the leads, we vary the width of the central scattering region [Fig. 1(a)]. This alteration leads to an energy level mismatch between the central region and the thermal leads, leading to the scattering of phonon modes. Figures 1(b) and 1(c) depict the transmission characteristics of the phonon modes from the left lead. In Fig. 1(b), the mode-resolved transmission function is projected onto the phonon band of the left lead. The transport of the TP edge modes are almost unaffected by backscattering, although the TC of other phonon modes is close to zero. Figure 1(c) displays the phonon transmission spectrum $\Xi(\omega)$ calculated using Caroli formula. $W_{1(3)}$ in the legend signifies that the narrowest width of the scattering region is 1(3) times of the width of a hexagonal lattice units [yellow-shaded range in Fig. 1(a)], while W_L corresponds to a perfect lattice with no scattering. Notably, the TCs for TP modes remain largely constant ($\Xi \sim 1$) as the width of the central scattering region increases, whereas the TCs for other phonon modes experience a moderate increase. The calculations indicate that the TP edge modes here are immune to backscattering.

For comparison, as shown in Fig. 2(a), we further consider a similar 2D device constructed of square lattice, the TP states of which have also been studied systematically in Ref. [2]. Here, we adopt values for the parameters similar to those in the hexagonal lattice above, i.e., $m_A = m_B = 1$, $\alpha_A = \alpha_B = 0.3$, $k_1 = 1$ and $k_2 = 0.5$. Figs. 2(b) and 2(c) display the transmission of phonon modes from the left thermal lead at varying widths of the central region. For example, the yellow-shaded range in Fig. 2(a) corresponds to a width of two square lattice units, denoted as W_2. Clearly, when the central scattering region has a width of W_2, not only is the transport of bulk modes affected, but there is also a notable scattering impact on the transport of the two TP edge states within the FBG around 1.5 ω_0. However, as the width of the central region increases from W_2 to W_{10}, the TCs of the TP edge modes gradually approach 1, while the TCs of the bulk phonon modes also increase to some extent. Figure 2(c) and its insets also provide a visual representation of this phenomenon.

The interesting contrast lies in the fact that there is almost no scattering when the TP modes transport in devices composed of a hexagonal lattice, whereas there is significant scattering in devices constructed with a square lattice. This seems to contradict the traditional idea that topological states are immune to backscattering, but it is not hard to explain this peculiar scattering phenomenon intuitively. Figure 3 presents schematic diagrams depicting the spatial distribution of TP edge states in the two different lattices with same frequency. For the square lattice, as the system

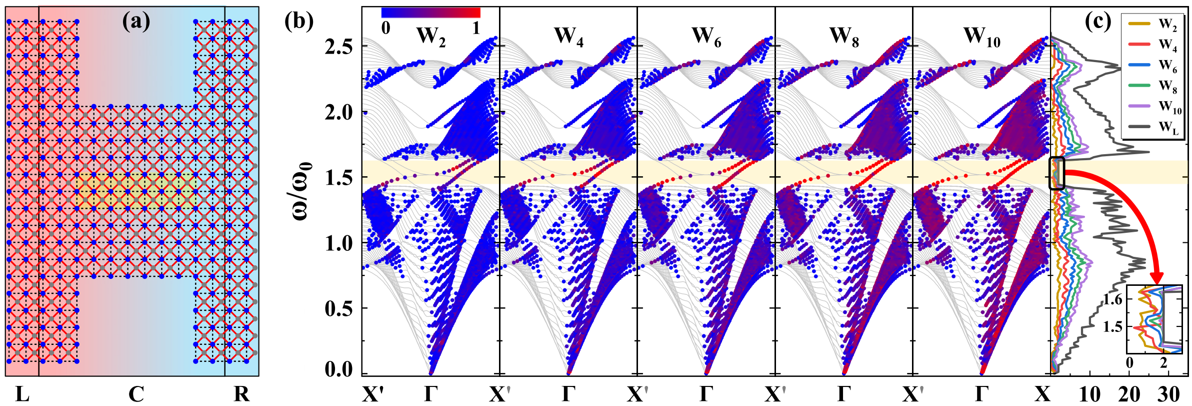

FIG. 2. Device transmission spectrum of square lattice. (a) Schematic of the two-dimensional device constructed from square lattice. Blue and gray points represent the sublattices with masses m_A and $m_B = m_A$, respectively. The red solid line and the black dashed line represent massless springs with stiffness k_1 and $k_2 = 0.5k_1$, respectively. The time-reversal ($\mathcal{T}$) symmetry is broken by introducing gyroscopic coupling [2]. (b) Mode-resolved transmission spectrum of the phonon modes from the left lead to the right lead under different width of the central scattering region. (c) Total transmission coefficient Ξ of the phonon modes from the left lead as a function of ω.

gradually narrows in the open boundary direction, the topological edge states at the left and right boundaries overlap in real space [Fig. 3(a)]. This overlap leads to a probability for the forward-propagating topological state at the left boundary to scatter with the backward-propagating topological state at the right boundary. In other words, during the overlap process, the backward-propagating topological states at the right boundary provide backscattering channels for the forward-propagating topological states at the left boundary. Moreover, as the extent of wave function overlap between the two topological edge modes increases, the probability of backscattering for this topological mode in the phonon device also increases.

However, the localization of TP edge states within the hexagonal lattice is extremely high [2]. Even when the width of the scattering region reduces to W_1, the edge states at two boundaries still have almost no overlap [Fig. 3(b)]. Hence, the TP edge states in hexagonal lattice can remain practically unaffected by backscattering. Therefore, we can draw the following conclusion: a phonon mode remains immune to backscattering in the absence of backscattering channels. In other words, even TP edge states have a probability of scattering if there are suitable backscattering channels.

By conducting a comparative analysis of the spring model devices, we derive the concept of a backscattering channel. These channels for a phonon mode correspond to other phonon eigenmodes with opposite group velocities, and their density distributions of states in real space overlap. The presence of backscattering channels ensures that a phonon mode will undergo backscattering. In the square lattice model, we achieve an overlap of topological modes from different boundaries in real space by narrowing the width of the central region of the device. Given that the topological modes at these boundaries exhibit opposite group velocities, we successfully establish backscattering channels for these topological modes. The topology patterns protected by $\mathcal{T}$ symmetry in the square lattice are thus backscattered.

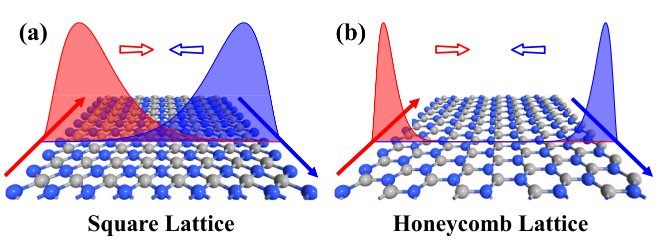

FIG. 3. Diagram of the wave function distribution of the topological phonon edge states with same frequency in real space.

III. ROBUSTNESS OF TOPOLOGICAL PHONONS IN GRAPHENE

Based on the understanding of phonon scattering mechanism, taking the ZGNR as an example, we further explore the transport behavior of TP states in nanomaterials. Recently, the nodal-ring phonons and Dirac phonons in bulk graphene have been observed experimentally [50]. However, the TP edge states of ZGNR in phonon band are located in LBGs [13,25,26]. The bulk modes may provide potential scattering channel for the TP modes. Therefore, it is needed to be reassessed for the robustness of TP edge states distributed in the LBG like ZGNR.

A. Force constant for ZGNR

We adopt the Vienna *ab initio* simulation package (VASP) [51,52] to perform the first-principles calculations based on density functional perturbation theory (DFPT) [53]. A vacuum layer of 20 Å is used for all the open boundary systems. The FCs of the $7 \times 7 \times 1$ supercell of graphene is extracted by using the PHONOPY code [54], and the FCs of ZGNRs and nanodevices are obtained by employing the phononic tight-binding method from the DFPT data.

The force constant (FC) matrix $\mathbf{\Phi}_A$ of a free-standing ZGNR must satisfy the acoustic sum rule (ASR) [26], i.e.,

$$\sum_{i(j)} \mathbf{\Phi}_{ij} = 0. \tag{5}$$

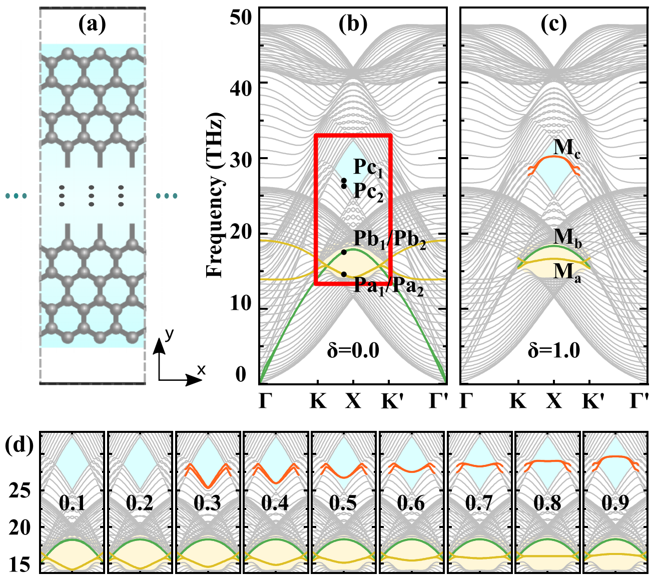

FIG. 4. Phonon band structures of zigzag graphene nanoribbon (ZGNR) in different edge local potential. (a) Schematic of the ZGNR. (b), (c), and (d) show the phonon band structures with different value of $\boldsymbol{\delta}$. The plotting range of each subplot in (d) corresponds to the region outlined by the red box in (a). Specifically, the frequency (y label) variation range for subplots in (d) is (13 THz, 33 THz), and the change in fractional coordinates of the wave vector (x label) is ($\mathbf{K} = 0.3$, $\mathbf{K}' = 0.7$).

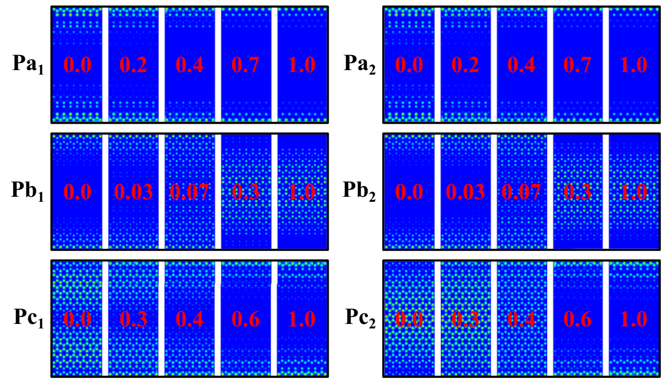

FIG. 5. Local density of state (LDOS) of the phonon states marked in Fig. 4(b) in different edge local potential. The red numbers in each subgraph represent the value of $\boldsymbol{\delta}$.

While another format of FC matrix ($\boldsymbol{\Phi}_U$), dealing like the electronic system, is shown in Ref. [13], i.e.,

$$\boldsymbol{\Phi}_{ii} = \boldsymbol{\Phi}_{jj}, i \neq j. \tag{6}$$

Here, atoms near the boundary experience external forces from surroundings of the system. In the majority of previous works, the FCs of open-boundary systems satisfy Eq. (6). The FC in this case has a format as follows:

$$\boldsymbol{\Phi} = \boldsymbol{\Phi}_A + \boldsymbol{\Phi}_L, \tag{7}$$

where $\boldsymbol{\Phi}_A$ represents the part that satisfies the ASR, and $\boldsymbol{\Phi}_L$ denotes the influence generated by a edge local potential.

Given the previous research on topological phonons, which involves two approaches regarding whether the force constant undergoes ASR correction, it is necessary to compare and discuss the robustness of topological phonons during the transport process under different degrees of ASR correction in order to obtain results of broader significance. Therefore, we assume $\boldsymbol{\Phi}_L = \boldsymbol{\delta} \times (\boldsymbol{\Phi}_U - \boldsymbol{\Phi}_A)$, such that when $\boldsymbol{\delta} = 0$, $\boldsymbol{\Phi}$ satisfies Eq. (5), and when $\boldsymbol{\delta} = 1$, $\boldsymbol{\Phi}$ satisfies Eq. (6). Consequently, we can investigate the transport characteristics of TP edge states as $\boldsymbol{\delta}$ varies from 0 to 1.

B. Phonon dispersion of ZGNR

As depicted in Fig. 4(a), we have constructed a ZGNR with a thickness of 20 layers, where the light blue background signifies that the atoms at the nanoribbon edges are subject to the influence of edge local potential. Next, we use Eq. (7) to establish the FCs of the nanoribbon, ensuring that when $\boldsymbol{\delta} = 1$, $\boldsymbol{\Phi}_{ii} = \boldsymbol{\Phi}^b_{kk}$, where $\boldsymbol{\Phi}^b_{kk}$ represents the on-site terms of bulk graphene atoms. Figures 4(b) and 4(c) show the phonon band structures of the ZGNR in the two specific states, $\boldsymbol{\delta} = 0$ and $\boldsymbol{\delta} = 1$, respectively. These results align well with previous works [13,26]. The TP edge states of interest, which are marked as $\mathbf{M_a}$, $\mathbf{M_b}$, and $\mathbf{M_c}$ in Fig. 4(c), are located within the region highlighted by a red rectangular frame in Fig. 4(b). Therefore, we conduct further calculations to investigate the evolution of the phonon band structure within the region corresponding to the red rectangular frame as $\boldsymbol{\delta}$ increases at intervals of 0.1 [Fig. 4(d)]. As $\boldsymbol{\delta}$ gradually increases from zero, the ASR is broken, leading to the disappearance of acoustic modes. Correspondingly, the edge states of topological acoustic phonons ($\mathbf{M_b}$) begin to merge into the bulk modes, as illustrated by the green lines in Fig. 4 [see Supplemental Material [49] for more details]. Conversely, in the vicinity of 30 THz, gradually emerging twofold degenerate edge modes ($\mathbf{M_c}$) appear within the LBG. Besides, it is worth noting that the optical topological modes ($\mathbf{M_a}$) near 15 THz persist throughout the process of $\boldsymbol{\delta}$ variation, even though their group velocities experience a reversal.

To provide a more intuitive representation of the changes in the edge states described above, as shown in Fig. 5, we proceed with calculations of the real-space local density of states (LDOS), which correspond to the black dots marked in Fig. 4(b). The corresponding wave vector for each of these states is $\boldsymbol{q} = 0.45$. To capture the crucial information about the LDOS variations, we perform different samplings for three sets of points with respect to $\boldsymbol{\delta}$. The red numbers represent the values of $\boldsymbol{\delta}$ corresponding to the LDOS. Obviously, as the value of $\boldsymbol{\delta}$ changes from 0 to 1, the LDOS of $\mathbf{Pa_1/Pa_2}$ remains distributed at the edge of the nanoribbon, and the LDOS of $\mathbf{Pb_1/Pb_2}$ transitions from an edge state to a bulk state, and the LDOS of $\mathbf{Pc_1/Pc_2}$ shifts from a bulk state to an edge state. Interestingly, the LDOS of Pc_1 and Pc_2 initially do not synchronize, which is due to the fact that these two modes have not yet degenerated when $\boldsymbol{\delta}$ is small.

C. Mode-resolved phonon transmission spectrum of ZGNR device

Finally, we compute the phonon transmission spectrum for the nanodevice shown in Fig. 6(a). Similar to the spring

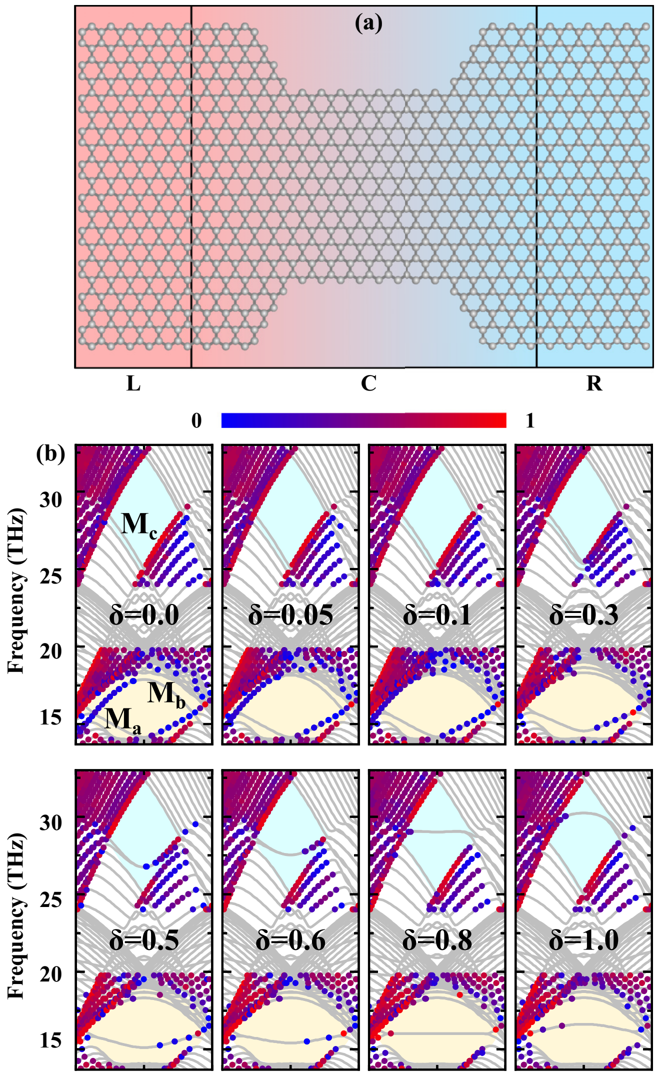

FIG. 6. Transmission spectrum of zigzag graphene nanoribbon (ZGNR) device. (a) Schematic diagram of the ZGNR device configuration. (b) Mode-resolved transmission spectrum of the phonon modes from the left thermal lead to the right thermal lead.

model discussed above, we introduce phonon scattering by reducing the width of the central region of the nanoribbon while ensuring that the edges of the device remain in a zigzag configuration. The TP edge states here are all situated within LBGs, making it impossible to get their TC from Caroli formula. Therefore, the use of the mode-resolved method is essential in this context. A cutoff radius of 6.5 Å is applied to the FCs of this device here. The principal layer of the thermal leads contains three primitive unit cells. Therefore, the wave vectors of the mode-resolved transmission spectrum will be in a folded Brillouin zone [44,48]. Here, we extend the band-unfolding technology and make it possible to show the transmission coefficient of every individual TP edge states. The unfolding technique for phonon mode-resolved transmission spectrum in this paper is also suitable for other crystalline materials. (see Supplemental Material [49] for more details.) By unfolding the Brillouin zone, we correlate the mode-resolved transmission spectrum with the phonon band structure of the thermal leads, as shown in Figs. 6(b) (see Supplemental Material [49] for more details.)

As shown in Fig. 6(b), when $\boldsymbol{\delta} = 0$, the TCs of $\mathbf{M_a}$ and $\mathbf{M_b}$ are very low, while the TC of $\mathbf{M_c}$ is quite high. When $\boldsymbol{\delta} = 1$, the TC of $\mathbf{M_b}$ have increased significantly. However, both $\mathbf{M_a}$ and $\mathbf{M_c}$ exhibit relatively low TCs. Moreover, due to their relatively small group velocities, there are only a few phonon modes contributing to transport in $\mathbf{M_a}$ and $\mathbf{M_c}$.

Through comparative analysis, we observe that $\mathbf{M_b}$ and $\mathbf{M_c}$ exhibit significantly higher TC values when transitioning into bulk states compared to when they are in the edge states. Conversely, $\mathbf{M_a}$ consistently maintains low TC values, likely due to its continuous presence as boundary states.

IV. DISCUSSIONS AND PERSPECTIVE

In this study, we initially discuss the behavior of topological phonon edge states protected by $\mathcal{T}$ symmetry in spring model devices under the gyroscopic effect. Through comparative analysis between honeycomb and square lattices, we extract the concept of backscattering channels. These channels correspond to eigenmodes with opposite group velocities, and their density distributions in real space overlap, leading to backscattering of phonon modes. We then delve into the robustness of TPs in ZGNRs through first-principles calculations, focusing on the scattering mechanism of backscattering channels. The TP edge modes in ZGNRs are located within LBGs, with numerous backscattering channels provided by co-frequency bulk modes, resulting in significant scattering during transport. It should be noted that both the spring model and first-principles calculations discussed here only account for elastic scattering, excluding considerations of anharmonic effects, electron-phonon coupling, magnon-phonon coupling, and similar factors.

In summary, we elucidate the scattering mechanism of TPs: they experience backscattering if suitable backscattering channels are present. In crystalline materials, achieving a strong $\mathcal{T}$ symmetry broken effect to open a full band gap in the phonon spectrum is challenging. Consequently, TP states in crystalline materials are typically found within LBGs in previous works. On the one hand, research on ZGNR devices reveals that TPs in crystalline materials generally lack robustness during transport. On the other hand, our calculations about the phonon band structure of ZGNR also indicate that the presence of edge local potentials can significantly affect the configuration and even the existence of TP edge modes. And for open-boundary nanostructures, the presence of dangling bonds typically leads to non-negligible edge local potentials. Therefore, the robustness of the existence and transport properties of TP edge states in crystalline materials may not be as strong as initially expected. Exploring TP states in FBG may be a effective way to avoid backscattering channels.

ACKNOWLEDGMENTS

This work was financially supported by the National Key Research and Development Program of Ministry of Science and Technology (2022YFA1402504) and by the National Natural Science Foundation of China (Grants No. 12374040, No. 11974106, and No. 12074112).

[1] L. Zhang, J. Ren, J.-S. Wang, and B. Li, Topological nature of the phonon Hall effect, Phys. Rev. Lett. **105**, 225901 (2010).

[2] P. Wang, L. Lu, and K. Bertoldi, Topological phononic crystals with one-way elastic edge waves, Phys. Rev. Lett. **115**, 104302 (2015).

[3] L. M. Nash, D. Kleckner, A. Read, V. Vitelli, A. M. Turner, and W. T. Irvine, Topological mechanics of gyroscopic metamaterials, Proc. Natl. Acad. Sci. USA **112**, 14495 (2015).

[4] Z. Yang, F. Gao, X. Shi, X. Lin, Z. Gao, Y. Chong, and B. Zhang, Topological acoustics, Phys. Rev. Lett. **114**, 114301 (2015).

[5] S. D. Huber, Topological mechanics, Nat. Phys. **12**, 621 (2016).

[6] Y. Liu, Y. Xu, S.-C. Zhang, and W. Duan, Model for topological phononics and phonon diode, Phys. Rev. B **96**, 064106 (2017).

[7] Y. Liu, C.-S. Lian, Y. Li, Y. Xu, and W. Duan, Pseudospins and topological effects of phonons in a Kekulé lattice, Phys. Rev. Lett. **119**, 255901 (2017).

[8] B. Xie, H. Liu, H. Cheng, Z. Liu, S. Chen, and J. Tian, Experimental realization of type-II Weyl points and Fermi arcs in phononic crystal, Phys. Rev. Lett. **122**, 104302 (2019).

[9] Y. Liu, X. Chen, and Y. Xu, Topological phononics: from fundamental models to real materials, Adv. Funct. Mater. **30**, 1904784 (2020).

[10] Y. Yang, H. Sun, J. Lu, X. Huang, W. Deng, and Z. Liu, Variable-order topological insulators, Commun. Phys. **6**, 143 (2023).

[11] X. Wang, T. Yang, Z. Cheng, G. Surucu, J. Wang, F. Zhou, Z. Zhang, and G. Zhang, Topological nodal line phonons: Recent advances in materials realization, Appl. Phys. Rev. **9**, 041304 (2022).

[12] Y. Jin, R. Wang, and H. Xu, Recipe for dirac phonon states with a quantized valley Berry phase in two-dimensional hexagonal lattices, Nano Lett. **18**, 7755 (2018).

[13] J. Li, L. Wang, J. Liu, R. Li, Z. Zhang, and X.-Q. Chen, Topological phonons in graphene, Phys. Rev. B **101**, 081403(R) (2020).

[14] Z. J. Chen, R. Wang, B. W. Xia, B. B. Zheng, Y. J. Jin, Y.-J. Zhao, and H. Xu, Three-dimensional dirac phonons with inversion symmetry, Phys. Rev. Lett. **126**, 185301 (2021).

[15] T. Zhang, Z. Song, A. Alexandradinata, H. Weng, C. Fang, L. Lu, and Z. Fang, Double-Weyl phonons in transition-metal monosilicides, Phys. Rev. Lett. **120**, 016401 (2018).

[16] H. Miao, T. T. Zhang, L. Wang, D. Meyers, A. H. Said, Y. L. Wang, Y. G. Shi, H. M. Weng, Z. Fang, and M. P. M. Dean, Observation of double Weyl phonons in parity-breaking FeSi, Phys. Rev. Lett. **121**, 035302 (2018).

[17] B. W. Xia, R. Wang, Z. J. Chen, Y. J. Zhao, and H. Xu, Symmetry-protected ideal type-II Weyl phonons in CdTe, Phys. Rev. Lett. **123**, 065501 (2019).

[18] J. Li, J. Liu, S. A. Baronett *et al.* Computation and data driven discovery of topological phononic materials, Nat. Commun. **12**, 1204 (2021).

[19] J. Li, Q. Xie, J. Liu, R. Li, M. Liu, L. Wang, D. Li, Y. Li, and X.-Q. Chen, Phononic Weyl nodal straight lines in MgB_2, Phys. Rev. B **101**, 024301 (2020).

[20] Y. Liu, N. Zou, S. Zhao, X. Chen, Y. Xu, and W. Duan, Ubiquitous topological states of phonons in solids: Silicon as a model material, Nano Lett. **22**, 2120 (2022).

[21] B. Peng, A. Bouhon, B. Monserrat, and R.-J. Slager, Phonons as a platform for non-Abelian braiding and its manifestation in layered silicates, Nat. Commun. **13**, 423 (2022).

[22] B. Zheng, B. Xia, R. Wang, Z. Chen, J. Zhao, Y. Zhao, and H. Xu, Ideal type-III nodal-ring phonons, Phys. Rev. B **101**, 100303(R) (2020).

[23] Y. J. Jin, Z. J. Chen, B. W. Xia, Y. J. Zhao, R. Wang, and H. Xu, Ideal intersecting nodal-ring phonons in bcc C_8, Phys. Rev. B **98**, 220103(R) (2018).

[24] S. Park, Y. Hwang, H. C. Choi *et al.*, Topological acoustic triple point, Nat. Commun. **12**, 6781 (2021).

[25] G. F. Lange, A. Bouhon, B. Monserrat, and R.-J. Slager, Topological continuum charges of acoustic phonons in two dimensions and the Nambu-Goldstone theorem, Phys. Rev. B **105**, 064301 (2022).

[26] Z.-K. Ding, Y.-J. Zeng, H. Pan, N. Luo, J. Zeng, L.-M. Tang, and K.-Q. Chen, Edge states of topological acoustic phonons in graphene zigzag nanoribbons, Phys. Rev. B **106**, L121401 (2022).

[27] F. F. Huang, P. Zhou, W. Q. Li, S. D. He, R. Tan, Z. S. Ma, and L. Z. Sun, Phononic second-order topological phase in the C_3N compound, Phys. Rev. B **107**, 134104 (2023).

[28] B. Li, L. Wang, and G. Casati, Thermal diode: Rectification of heat flux, Phys. Rev. Lett. **93**, 184301 (2004).

[29] Y. Liu, Y. Xu, and W. Duan, Three-dimensional topological states of phonons with tunable pseudospin physics, Research **2019** (2019).

[30] Z.-Y. Ong and C. H. Lee, Transport and localization in a topological phononic lattice with correlated disorder, Phys. Rev. B **94**, 134203 (2016).

[31] J. P. Mathew, J. d. Pino, and E. Verhagen, Synthetic gauge fields for phonon transport in a nano-optomechanical system, Nat. Nanotechnol. **15**, 198 (2020).

[32] G. Xu, Y. Yang, X. Zhou *et al.*, Diffusive topological transport in spatiotemporal thermal lattices, Nat. Phys. **18**, 450 (2022).

[33] G. Xu, W. Li, X. Zhou, H. Li, Y. Li, S. Fan, S. Zhang, D. N. Christodoulides, and C.-W. Qiu, Observation of Weyl exceptional rings in thermal diffusion, Proc. Natl. Acad. Sci. USA **119**, e2110018119 (2022).

[34] H. Ren, T. Shah, H. Pfeifer, C. Brendel, V. Peano, F. Marquardt, and O. Painter, Topological phonon transport in an optomechanical system, Nat. Commun. **13**, 3476 (2022).

[35] S.-X. Xia, D. Zhang, X. Zhai, L.-L. Wang, and S.-C. Wen, Phase-controlled topological plasmons in 1D graphene nanoribbon array, Appl. Phys. Lett. **123**, 101102 (2023).

[36] J. Cui, E. V. Boström, M. Ozerov, F. Wu, Q. Jiang, J.-H. Chu, C. Li, F. Liu, X. Xu, A. Rubio *et al.*, Chirality selective magnon-phonon hybridization and magnon-induced chiral phonons in a layered zigzag antiferromagnet, Nat. Commun. **14**, 3396 (2023).

[37] H. Pan, L.-M. Tang, and K.-Q. Chen, Quantum mechanical modeling of magnon-phonon scattering heat transport across three-dimensional ferromagnetic/nonmagnetic interfaces, Phys. Rev. B **105**, 064401 (2022).

[38] H. Pan, Z.-K. Ding, B.-W. Zeng, N.-N. Luo, J. Zeng, L.-M. Tang, and K.-Q. Chen, *Ab initio* Boltzmann approach to coupled magnon-phonon thermal transport in ferromagnetic crystals, Phys. Rev. B **107**, 104303 (2023).

[39] J. Lu, W. Deng, X. Huang, M. Ke, and Z. Liu, Non-Hermitian topological phononic metamaterials, Adv. Mater. 2307998 (2023).
[40] T. Yu, J. Zou, B. Zeng, J. Rao, and K. Xia, Non-Hermitian topological magnonics, Phys. Rep. **1062**, 1 (2024).
[41] R. He, D. Wang, N. Luo, J. Zeng, K.-Q. Chen, and L.-M. Tang, Nonrelativistic spin-momentum coupling in antiferromagnetic twisted bilayers, Phys. Rev. Lett. **130**, 046401 (2023).
[42] D. Liu, J. Zeng, X. X. Jiang, L. Tang, and K. Chen, Exact first-principles calculation reveals universal Moiré potential in twisted two-dimensional materials, Phys. Rev. B **107**, L081402 (2023).
[43] Z.-Y. Ong and G. Zhang, Efficient approach for modeling phonon transmission probability in nanoscale interfacial thermal transport, Phys. Rev. B **91**, 174302 (2015).
[44] Z.-Y. Ong, Atomistic s-matrix method for numerical simulation of phonon reflection, transmission, and boundary scattering, Phys. Rev. B **98**, 195301 (2018).
[45] C. Caroli, R. Combescot, P. Nozieres, and D. Saint-James, Direct calculation of the tunneling current, J. Phys. C **4**, 916 (1971).
[46] J.-S. Wang, J. Wang, and J. Lü, Quantum thermal transport in nanostructures, Eur. Phys. J. B **62**, 381 (2008).
[47] S. Sadasivam, U. V. Waghmare, and T. S. Fisher, Phonon-eigenspectrum-based formulation of the atomistic Green's function method, Phys. Rev. B **96**, 174302 (2017).
[48] X. Chen, Y. Xu, J. Wang, and H. Guo, Valley filtering effect of phonons in graphene with a grain boundary, Phys. Rev. B **99**, 064302 (2019).
[49] See Supplemental Material at http://link.aps.org/supplemental/10.1103/PhysRevB.109.245104 for more details about the computational methods of atomistic s-matrix method and band unfolding, phonon band structures of zigzag graphene nanoribbon and Si(111) surface, which includes Figs. S1– S5 and Refs. [43,44,48].
[50] J. Li, J. Li, J. Tang, Z. Tao, S. Xue, J. Liu, H. Peng, X.-Q. Chen, J. Guo, and X. Zhu, Direct observation of topological phonons in graphene, Phys. Rev. Lett. **131**, 116602 (2023).
[51] G. Kresse and J. Furthmüller, Efficiency of *ab initio* total energy calculations for metals and semiconductors using a plane-wave basis set, Comput. Mater. Sci. **6**, 15 (1996).
[52] G. Kresse and J. Furthmüller, Efficient iterative schemes for *ab initio* total-energy calculations using a plane-wave basis set, Phys. Rev. B **54**, 11169 (1996).
[53] S. Baroni, S. De Gironcoli, A. Dal Corso, and P. Giannozzi, Phonons and related crystal properties from density-functional perturbation theory, Rev. Mod. Phys. **73**, 515 (2001).
[54] A. Togo and I. Tanaka, First principles phonon calculations in materials science, Scr. Mater. **108**, 1 (2015).